# Retrieval of Solar-induced Chlorophyll Fluorescence from Satellite Measurements: Comparison of SIF between TanSat and OCO-2

Lu Yao[1,2], Yi Liu[1,3], Dongxu Yang[1,3], Zhaonan Cai[1], Jing Wang[1], Chao Lin[4], Naimeng Lu[5], Daren Lyu[1], Longfei Tian[6], Maohua Wang[3], Zengshan Yin[6], Yuquan Zheng[4], Sisi Wang[7]

[1]Key Laboratory of Middle Atmosphere and Global Environment Observation, Institute of Atmospheric Physics, Chinese Academy of Sciences, No. 40, Huayan Li, Chaoyang District, Beijing 100029, China
[2]University of Chinese Academy of Sciences, No. 19A, Yuquan Lu, Shijing Shan District, Beijing 100049, China
[3]Shanghai Advanced Research Institute, Chinese Academy of Sciences, Shanghai 201210, China
[4]Changchun Institute of Optics, Fine Mechanics and Physics, Changchun 130033, China
[5]National Satellite Meteorological Center, China Meteorological Administration, Beijing 100081, China
[6]Shanghai Engineering Center for Microsatellites, Shanghai 201203, China
[7]National Remote Sensing Center of China, Beijing 100036, China

*Correspondence to*: Dongxu Yang (yangdx@mail.iap.ac.cn)

**Abstract.** Solar-induced chlorophyll fluorescence (SIF) is emitted during photosynthesis in plant leaves. It constitutes a small additional offset to reflected radiance and can be observed by sensitive instruments ~~that~~ with high signal-to-noise ratio and spectral resolution. The Chinese global carbon dioxide monitoring satellite (TanSat)~~, as its mission~~, acquires greenhouse gas column density. The advanced technical characteristics of the ~~hyper-spectrum~~ grating spectrometer (ACGS) onboard TanSat enable SIF retrieval from ~~space~~ observations in the $O_2$-A band. In this study, one-year SIF data for each sounding was retrieved from Orbiting Carbon Observatory-2 (OCO-2) and TanSat measurements using the IAPCAS/SIF algorithm. A comparison between the SIF results retrieved from OCO-2 spectra and the official OCO-2 SIF product (OCO2_Level 2_Lite_SIF.8r) shows their strong linear relationship ($R^2 > 0.85$) and suggests the reliability of the SIF retrieval algorithm. The global distribution showed that the SIF retrieved from the two satellites shared the same spatial pattern for all seasons with the ~~gridded~~ SIF difference less than 0.3 W m$^{-2}$ μm$^{-1}$ sr$^{-1}$, and they also agreed well with the official OCO-2 SIF product with the ~~the~~ difference less than 0.2 W m$^{-2}$ μm$^{-1}$ sr$^{-1}$. The retrieval uncertainty of seasonal-gridded TanSat SIF is less than 0.03 W m$^{-2}$ μm$^{-1}$ sr$^{-1}$ whereas the uncertainty of each sounding ranges from 0.1 to 0.6 W m$^{-2}$ μm$^{-1}$ sr$^{-1}$. The relationship between annually-averaged SIF products and FLUXCOM gross primary productivity (GPP) was also estimated for six vegetation types in a $1° \times 1°$ grid over the globe, indicating that the SIF data from the two satellites have the same potential in quantitatively characterizing ecosystem productivity. The spatiotemporal consistency between TanSat and OCO-2 and their comparable data quality make the comprehensive usage of the two mission products possible. Data supplemented by TanSat observations are expected to contribute to the development of global SIF maps with more spatiotemporal detail, which will advance global research on vegetation photosynthesis.

## 1 Introduction

Terrestrial vegetation accounts for a large part of the ecosystem, with its photosynthesis and respiration processes playing important roles in the global carbon cycle. Incoming radiation is absorbed, reflected, and/or transmitted by plant leaves. A portion of the absorbed radiation is used by the chlorophyll in plant leaves for carbon fixation, while the rest is either dissipated as heat or re-emitted as solar-induced chlorophyll fluorescence (SIF) at longer wavelengths (Frankenberg et al., 2011a, 2014). In contrast to the traditional remotely sensed vegetation indices obtained from some studies (Frankenberg et al., 2011b; Guanter et al., 2014; Li et al., 2018; Sun et al., 2017a; Yang et al., 2015; Zhang et al., 2014), SIF offers the potential to measure photosynthesis activity and gross primary production (GPP), due to the strong correlation between these measures (Frankenberg et al., 2011b; Guanter et al., 2012, 2014). The fluorescence emission (Fs) adds a low-intensity radiance less than 10 W m$^{-2}$ μm$^{-1}$ sr$^{-1}$ and fills in the solar absorption features of the reflected spectrum (Frankenberg et al., 2011a). The filling-in effect of the solar lines (Fraunhofer lines) is the basic principle applied to measure SIF from space using the capabilities of hyperspectral observation (Frankenberg et al., 2011b; Guanter et al., 2012).

The first attempt at SIF research based on space-based observations was performed using images acquired by the Medium Resolution Imaging Spectrometer (MERIS) onboard the ENVIronmental SATellite (ENVISAT) (Guanter et al., 2007). This led to a new idea for conducting SIF studies on a global scale. The first global SIF map was retrieved with high-resolution spectra from the Greenhouse-gases Observing SATellite (GOSAT) (Joiner et al., 2011; Frankenberg et al., 2011b). After that, SIF retrievals were implemented from a variety of satellite measurements, such as those from the Global Ozone Monitoring Experiment-2 (GOME-2) instruments onboard meteorological operational satellites, SCIAMACHY on board ENVISAT, and Orbiting Carbon Observatory-2 (OCO-2) (Joiner et al., 2016; Köhler et al., 2015). The TROPOspheric Monitoring Instrument (TROPOMI) on board Sentinel 5 Precursor (S-5P) provides more efficient SIF observations in terms of global coverage and new opportunities for exploring the application potential of SIF data in the terrestrial biosphere as well as in climate research (Doughty et al., 2019; Köhler et al., 2018b). Furthermore, an upcoming European Space Agency mission called FLuorescence EXplorer (FLEX), the first satellite dedicated to SIF emission observation, will launch in the middle of 2024 (Drusch et al., 2017). Many studies on SIF applications have been initiated with the accumulation of SIF products in recent years. The responses of satellite-measured SIF to environmental conditions have been applied to drought dynamics monitoring and regional vegetation water stress estimation (Lee et al., 2013; Sun et al., 2015; Yoshida et al., 2015). As a proxy of photosynthesis, SIF acts as a powerful constraint parameter in estimating carbon exchange in an ecosystem between the atmosphere, ocean, and soil; as such, the analysis of the relationship between SIF and GPP has become an important research topic (Li et al., 2018; Köhler et al., 2018a; Sun et al., 2017a; Zhang et al., 2018). The strong linear relationship between them paves the way for improving terrestrial ecosystem model simulation of GPP, along with consequent improvement of global carbon flux estimation (MacBean et al., 2018; Yin et al., 2020). GPP estimations based on satellite-measured SIF have proven to be an effective method validated by in-situ flux observations (Joiner et al., 2018; Qiu et al., 2020). However, uncertainty in the factors that determine the relationship between SIF and GPP still exists and is a key

68  limitation in the application of SIF to flux estimation. Based on multi-satellite SIF products, eddy covariance flux tower

69  observations, and ecological models, the relationship between SIF and GPP under different environmental conditions has

70  been discussed in a number of studies to analyze the dominant factors for the growing status of different biomes, such as

71  temperature, soil moisture, and vegetation types (Chen et al., 2020; Doughty et al., 2019; Li et al., 2020; Qiu et al., 2020; Yin

72  et al., 2020).

73  The Chinese global carbon dioxide monitoring satellite (TanSat) was launched in December 2016. Aiming at acquiring $CO_2$

74  concentrations as OCO-2, TanSat flies in a sun-synchronous orbit at approximately 700 km in height with a 16-day repeat

75  cycle and an equator crossing time of ~1:30 p.m. local time (Cai et al., 2014; Liu et al., 2018; Yang et al., 2018). Onboard

76  TanSat, the hyperspectral Atmospheric Carbon-dioxide Grating Spectrometer (ACGS) is designed to separately record solar

77  backscatter spectra in three channels centered at 0.76 μm ($O_2$-A band), 1.61 μm (weak $CO_2$ absorption band), and 2.06 μm

78  (strong $CO_2$ absorption band). With the recorded spectra, many Optimal Estimation Method (OEM) full physics retrieval

79  algorithms have been developed and applied for $XCO_2$ retrievals (Boesche et al., 2009; Butz et al., 2009, 2011; O'Dell et al.,

80  2012; Reuter et al., 2010; Yang et al., 2015b; Yoshida et al., 2011, 2013). The Institute of Atmospheric Physics Carbon

81  Dioxide Retrieval Algorithm for Satellite Remote Sensing (IAPCAS) algorithm has been applied for TanSat retrieval (Yang

82  et al., 2018; Yang et al., 2021) and was also previously tested on GOSAT and OCO-2 missions (Yang et al., 2015b).

83  However, the fluorescence feature causes substantial biases when retrieving surface pressure and scattering parameters from

84  the $O_2$-A band, and the associated errors propagate into the $XCO_2$ retrievals. In previous $XCO_2$ retrieval, the surface

85  emissions were well modeled as a continuum zero offset of the $O_2$-A band to reduce errors (Frankenberg et al., 2011a, 2012;

86  Butz et al., 2009, 2010; Joiner et al., 2012). The high spectral resolution of ~0.044 nm and a signal-to-noise ratio of ~360 in

87  the $O_2$-A band makes it possible to obtain SIF from space measurements, with a spatial resolution of 2 km × 2 km in nadir

88  mode (Liu et al., 2018).

89  Various approaches have been used to infer SIF from satellite measurements (Frankenberg et al., 2011b, 2014a, 2014b;

90  Guanter et al., 2007, 2012, 2015; Joiner et al., 2011, 2013, 2016; Köhler et al., 2015, 2018b). The SIF signal induces a

91  filling-in effect of solar lines, which can be used for SIF retrieval, as the fractional depth of solar Fraunhofer lines does not

92  change during radiation transmission in the atmosphere. To recognize the filling-in features by SIF, high-resolution spectra

93  and an instrument spectral response function (ISRF) are required to describe subtle changes in the spectral absorption lines.

94  With the detailed spectral features, a method was developed based on solar line fitting and the Beer-Lambertian law. This

95  method is robust and accurate when the spectrum is out of the influence of telluric absorptions, even in the presence of

96  aerosols (Frankenberg et al., 2011a; Joiner et al., 2011); in the current study, this method was applied to develop the

97  IAPCAS/SIF algorithm. Another SIF retrieval method is the data-driven algorithm based on the singular value

98  decomposition (SVD) technique (Joiner et al., 2011; Guanter et al., 2012), which has been broadly applied in GOSAT, OCO-

99  2, TanSat and TROPOMI SIF retrieval (Joiner et al., 2011; Guanter et al., 2012, 2015; Frankenberg et al., 2014a; Du et al.,

100 2018; Köhler et al., 2018b). In the data-driven method, the spectrum is represented as a linear combination of the SIF signal

101 and several singular vectors that are trained from non-fluorescent scenes by SVD; thus, the SIF signal can be obtained with

102  linear least-squares fitting  (Du et al., 2018; Guanter et al., 2012). The first TanSat SIF map was obtained by the SVD
103  method (Du et al., 2018). In a previous study, a new TanSat SIF product retrieved by IAPCAS/SIF algorithm was introduced
104  and the two kinds of TanSat SIF product by IAPCAS/SIF and SVD methods were compared. The preliminary comparison
105  between the two TanSat SIF products shows that the two SIF products share a similar global pattern and signal magnitude
106  for all seasons while different biases still exist in four seasons (Yao et al., 2021). The different biases in four seasons may be
107  caused by the different training samples of the SVD method, which indicates that the training samples have a significant
108  impact on the retrieval results. In order to obtain stable SIF data products from TanSat and other subsequent satellite
109  missions, it is particularly important to establish a stable and high-precision SIF inversion algorithm. To detailed validate the
110  IAPCAS/SIF algorithm and test the potential of comprehensive usage of multi-satellites SIF data in analysis, in this study,
111  we detailed the TanSat SIF retrieval using the IAPCAS/SIF algorithm and made a comparison of SIF products between
112  TanSat and OCO-2 in variety of temporal-spatial scales, although a preliminary test was shown in previous work.

113  **2 Data and retrieval algorithm**

114  **2.1 Retrieval Principle and Method**

115  We used TanSat version 2 Level 1B (L1B) nadir-mode earth observation data in the retrieval process. The measurements
116  covered the period from March 2017 to February 2018. Polarized radiance in the $O_2$-A band with a spectral resolution of
117  0.044 nm was provided in the L1B data, and two micro-windows near 757 nm (758.3-759.2 nm) and 771 nm (769.6-770.3
118  nm) were chosen to retrieve the top-of-atmosphere (TOA) SIF while avoiding the contamination from strong lines of
119  atmospheric gas absorption. The retrieval was independent for each micro-window as shown in Figure 1. To avoid
120  duplication of information, we use the SIF product at 757 nm as the example in the analysis.
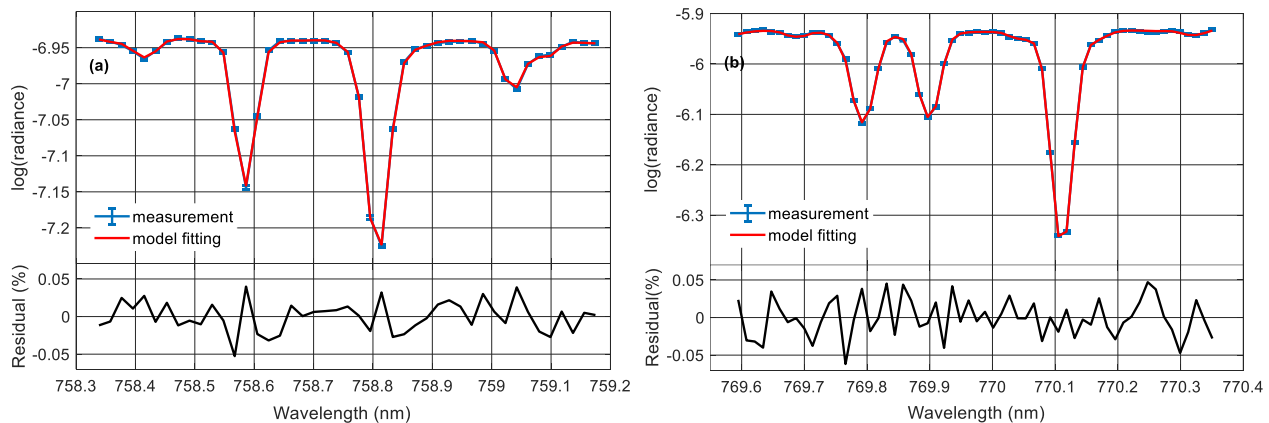


121
122  **Figure 1: The fitted spectra and residuals for the (a) 757 nm and (b) 771 nm micro-windows of TanSat measurement. The error**
123  **bar of the measured spectra depicts the estimated precision of each TanSat sounding.**

124

4

125  Filling-in on solar lines by chlorophyll fluorescence in the $O_2$-A band can be detected in the hyperspectral measurements

126  from TanSat. This effect on spectral radiance is different from the impact of atmospheric and surface processes, e.g.,

127  scattering and absorption. For example, scattering by aerosols and clouds does not change the relative depth of clear solar

128  lines, unlike the SIF emission signal. We applied the differential optical absorption spectroscopy (DOAS) technique to

129  IAPCAS/SIF algorithm for TanSat measurement (Frankenberg, 2014b; Sun et al., 2018).

130  The TOA spectral radiance ($L_{TOA}^\lambda$) at wavelength $\lambda$ can be represented as follows:

131  $$L_{TOA}^\lambda = I_t^\lambda \cdot \mu_0 \cdot \left(\rho_0^\lambda + \frac{\rho_s^\lambda \cdot T_\downarrow^\lambda \cdot T_\uparrow^\lambda}{\pi}\right) + F_{TOA}^\lambda \qquad (1)$$

132  where $I_t^\lambda$ is the incident solar irradiance at the TOA, $\mu_0$ is the cosine of the solar zenith angle (SZA), $\rho_0^\lambda$ is atmospheric path

133  reflectance, $\rho_s^\lambda$ is surface reflectance, and $T_\downarrow^\lambda$ and $T_\uparrow^\lambda$ are the total atmospheric transmittances along the light-path in the

134  downstream and upstream directions, respectively. $F_{TOA}^\lambda$ is the SIF radiance at TOA.

135  The first term on the right of Eq. (1) represents the transmission process of solar radiance. In the micro-windows used in SIF

136  retrieval, gas absorption is very weak and smooth, and hence, the atmosphere term $\mu_0 \cdot \left(\rho_0^\lambda + \frac{\rho_s^\lambda \cdot T_\downarrow^\lambda \cdot T_\uparrow^\lambda}{\pi}\right)$ can be simplified to a

137  low-order polynomial that varies with $\lambda$ (Joiner et al., 2013; Sun et al., 2018); this is always valid as long as the spectrum

138  fitting range is out of sharp atmospheric absorptions. In the retrieval, the spectral radiance measurement was converted to

139  logarithmic space by the instrument and the radiative transfer process $f(F_s^{rel}, \boldsymbol{a})$ was represented as follows:

140  $$f(F_s^{rel}, \boldsymbol{a}) = log(< I_t + F_s^{rel} >) + \sum_{i=0}^{n} a_i \cdot \lambda^i \qquad (2)$$

141  where $< >$ denote the convolution with the ISRF from line-by-line spectra. The polynomial coefficient $\boldsymbol{a}$ determines the

142  wavelength dependence polynomial for the atmosphere term; in the retrieval, we used a second-order polynomial ($n = 2$).

143  The radiance is normalized to the continuum level; hence, $I_t$ is a normalized disk-integrated solar transmission model, and

144  $F_s^{rel}$ is the normalized relative SIF. In the micro-window, SIF was regarded as a constant signal due to its small changes.

145  Although the atmospheric gas absorption was very weak in the micro-window, the weak absorption and the far-wing effects

146  ($O_2$ lines) can still change spectral features, which induces errors in spectrum fitting. In other physical-based retrievals, the

147  surface pressure data of the European Centre for Medium-Range Weather Forecasts (ECMWF) is usually used as the true

148  surface pressure to simulate the molecular absorption cross-section. However, there is still a difference between the true

149  surface pressure and the model surface pressure, so we introduced a factor here to reduce the influent of the inaccurate

150  surface pressure. In IAPCAS/SIF algorithm, we used the ECMWF interim surface pressure ($0.75° \times 0.75°$) to estimate $O_2$

151  absorption firstly and then modified the absorption feature by a scale factor. The scale factor is obtained simultaneously in

152  SIF retrieval to reduce the error induced by the uncertainty in surface pressure. As described by Yang (2020), there is also a

153  continuum feature in TanSat L1B data that needs to be considered for the high-quality fitting of the $O_2$-A band. However, in

154  this study, this continuum feature was not corrected, as the impact of such a smooth continuum variation in the micro-

155  window is weak and the polynomial continuum model is capable of compensating for most of this effect.

156  The state vector ~~list in the retrieval~~ includes the relative SIF signal $F_s^{rel}$, a wavenumber shift, the scale of $O_2$ column

157  absorption ~~for surface pressure correction~~, and coefficients of the polynomial. The continuum level radiance $I_{cont}$ within the

158  fitting window is calculated using the radiance outside the absorption features in the micro-window and is then used for the

159  actual SIF signal calculation thus: $F = F_s^{rel} \cdot I_{cont}$.

160  In the IAPCAS/SIF algorithm, we used an OEM for state vector optimization in the retrieval process. Unlike $XCO_2$ retrieval,

161  SIF retrieval employs a state vector with fewer elements and a much simpler forward model, so there is no need to perform

162  complex radiation transmission calculations. Considering the low complexity of SIF retrieval, the Gauss-Newton method

163  was applied ~~in inversion~~ iteratively to find the optimal solution.

## 2.2 Bias Corrections

165  A systematic error remains in the raw SIF retrieval output if no bias correction is performed; similar results have been

166  reported in GOSAT and OCO-2 SIF retrieval studies (Frankenberg et al., 2011a, 2011b; Sun et al., 2018). This is because the

167  SIF signal is weak (e.g., typically ~1-2% of the continuum level radiance), which means that even a small issue in the

168  measurement, such as a zero-offset caused by radiometric calibration error, could induce significant bias. Unfortunately, the

169  lack of knowledge on in-flight instrument performance makes it difficult to perform a direct systematic bias correction in the

170  measured spectrum. In the retrieval, a continuum level radiance bin fit was used to estimate the bias. The bins have a

171  continuum level radiance interval of 5 W $m^{-2}$ $\mu m^{-1}$ $sr^{-1}$. In each bin, the mean bias was estimated using all non-fluorescence

172  measurements, and a piecewise linear function was built from the mean bias of each continuum level radiance interval.

173  The non-fluorescence soundings that were used in the bias estimation were based on the dataset "sounding_landCover" in

174  TanSat L1B data. This dataset depends on the MODIS land cover product and provides a scheme consisting of 17 land cover

175  classifications defined by the International Geosphere-Biosphere Programme. These retrieved measurements marked as

176  "snow and ice," "barren," and "sparsely vegetated" were chosen to estimate the bias. Calibrations compensated for most of

177  the instrument degradations, but this alone was not perfect. To reduce the impact from the remaining minor discrepancies,

178  we built the bias correction function daily to obtain bias for each sounding via interpolation of the continuum level radiance

179  (Sun et al., 2017b, 2018).

180  The bias curves shown in Figure 2 differ significantly between TanSat and OCO-2. This is mostly due to the differences in

181  instrument performance and radiometric calibration. In general, the TanSat bias curves exhibited two peaks at radiance levels

182  of approximately 40 and 125 W $m^{-2}$ $\mu m^{-1}$ $sr^{-1}$, separately, and most biases were larger than 0.015. For OCO-2, the curves

183  dropped sharply at low radiance levels, reaching the valley at a radiance level of approximately 40 W $m^{-2}$ $\mu m^{-1}$ $sr^{-1}$, and then

184  increased slowly with the radiance level.
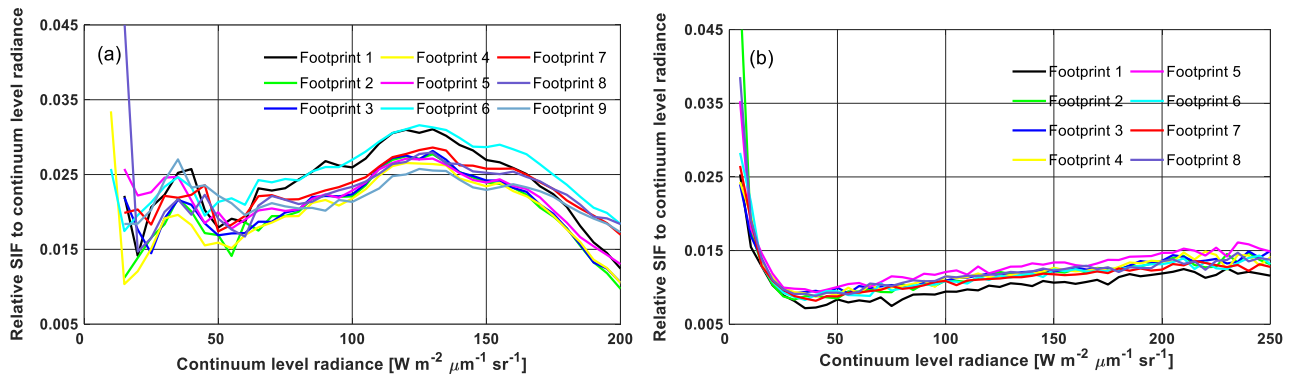
**Figure 2: Variations in the bias correction curves of continuum level radiance from (a) TanSat on July 7, 2017, and (b) Orbiting Carbon Observatory-2 (OCO-2) on June 16, 2017. The different colors in the legend present different footprints of the satellite frame.**

## 2.3 Data Quality Controls

Only data that passed quality control were used in further applications. There were two data quality control processes for the SIF products: pre-screening and post-screening. Pre-screening focused mainly on cloud screening; only cloud-free measurements were used in SIF retrieval. A surface pressure difference (SPD), defined as:

$$\Delta P_0 = |P_{retrieval} - P_{ECMWF}| \tag{3}$$

was used to evaluate cloud contamination along with a chi-square test

$$\chi^2 = \sum \frac{(y_{sim} - y_{obs})^2}{y_{noise}^2} \tag{4}$$

where $y_{sim}$, $y_{obs}$, and $y_{noise}$ represent the model fitting spectrum, observation spectrum, and spectrum noise, respectively. $P_{retrieval}$ is the apparent surface pressure obtained from $O_2$-A band surface pressure retrieval, assuming a single scattering atmosphere. $P_{ECMWF}$ is the ECMWF interim ($0.75° \times 0.75°$) surface pressure. A "cloud-free" measurement was required to simultaneously satisfy an SPD of less than 20 hPa and a $\chi^2$ value of less than 80. Here, post-screening was applied to filter out "bad" retrievals; this screening process involved the following steps: (1) SIF retrievals with reduced $\chi^2$ ($\chi_{red}^2$) values ranging from 0.7 to 1.3 were considered "good" fitting, (2) continuum level radiance outside the range of 15 ~ 200 W m$^{-2}$ µm$^{-1}$ sr$^{-1}$ was screened out to avoid scenes too bright or too dark, and (3) soundings with the SZA higher than 60° were also filtered out.

## 2.4 IAPCAS versus IMAP-DOAS OCO-2 SIF Retrieval

Before applied to TanSat retrievals, we tested the IAPCAS/SIF algorithm on the OCO-2 L1B data first (OCO2_L1B_Science.8r) and then compared the retrieval results with the OCO-2 L2 Lite SIF product (OCO2_Level 2_Lite_SIF.8r) retrieved by the Iterative Maximum A Posteriori-Differential Optical Absorption Spectroscopy (IMAP-DOAS) algorithm (Frankenberg, 2014b). The Lite product provides the SIF value for each sounding ~~on a daily basis~~ and hence the SIF comparison could be performed on the sounding scale for each month.

Table 1 displays the relationship of OCO-2 SIF values between the IAPCAS/SIF and IMAP-DOAS at 757 nm micro-window for each month. Overall, the two SIF products were in good agreement. The linear fitting of the two SIF products suggests that they are highly correlated, as indicated by the strong linear relationship with $R^2$ mostly larger than 0.85 and the root mean square error (RMSE) of about 0.2 W m$^{-2}$ μm$^{-1}$ sr$^{-1}$. Good consistency between the two SIF products implies the reliability of the IAPCAS/SIF algorithm; thus, it was further applied to TanSat SIF retrieval. However, there was still a small bias in the comparisons, which was due, most likely, to the impact of differences in the bias correction method, retrieval algorithm, and fitting window.

**Table 1:** Summary of the relationship between the Institute of Atmospheric Physics Carbon Dioxide Retrieval Algorithm for Satellite Remote Sensing (IAPCAS) OCO-2 and Iterative Maximum A Posteriori-Differential Optical Absorption Spectroscopy (IMAP-DOAS) OCO-2 solar-induced chlorophyll fluorescence (SIF) products at 757nm micro-window.

| month | Number of soundings | Slope | Intercept | $R^2$ | RMSE/ W m$^{-2}$ μm$^{-1}$ sr$^{-1}$ |
|---|---|---|---|---|---|
| 2017/03 | 1097277 | 0.85 | 0.034 | 0.86 | 0.18 |
| 2017/04 | 1119464 | 0.86 | 0.045 | 0.87 | 0.19 |
| 2017/05 | 1054235 | 0.88 | 0.041 | 0.88 | 0.19 |
| 2017/06 | 1014848 | 0.91 | 0.032 | 0.90 | 0.19 |
| 2017/07 | 965309 | 0.92 | 0.011 | 0.91 | 0.19 |
| 2017/09 | 211219 | 0.88 | 0.005 | 0.81 | 0.23 |
| 2017/10 | 473359 | 0.88 | 0.031 | 0.88 | 0.17 |
| 2017/11 | 579009 | 0.87 | 0.022 | 0.85 | 0.19 |
| 2017/12 | 645134 | 0.87 | 0.020 | 0.88 | 0.16 |
| 2018/01 | 788655 | 0.87 | 0.019 | 0.88 | 0.17 |
| 2018/02* | 629995 | 0.86 | 0.024 | 0.87 | 0.18 |

* Due to the lack of OCO-2 measurements in August 2017, the comparison is only performed for 11 months.

## 3 Results and Discussion

### 3.1 Comparison between TanSat and OCO-2 SIF Measurements

The comparison between TanSat and OCO-2 SIF Measurements is a useful and powerful method for further verification of the IAPCAS/SIF algorithm. The reason for adopting OCO-2 data is that OCO-2 and TanSat have similar observation modes, including scanning method, transit time, spatial resolution, spectral resolution, and spectral range. The similarities mean that the SIF product from the two satellite missions can be directly compared. Directly comparing OCO-2 and TanSat SIF measurements could provide information on joint data application at the sounding scale for further studies. However, an identical sounding overlap barely exists because the two satellites often have different nadir tracks on the ground, which is induced by the different temporal and spatial intervals of the two satellite missions. Fortunately, the ground tracks of the two satellites were relatively close from April 17 to April 23, 2017. A couple of overlapping orbits were found in the measurements obtained from Africa with the orbit number of 1733 from TanSat and 14890a from OCO-2 (Figure 3). In the

232 comparison, the OCO2_Level 2_Lite_SIF.8r product was used to present the SIF emission over the study area. These

233 overlapping measurements encompassed multiple land cover types, in which the SIF varied within an acceptable time

234 difference (<5 min).

235 Overall, measurements from the two satellites indicated SIF variation with land cover type. The SIF emission over evergreen

236 broadleaf forests was larger than that over savannas, and grasslands exhibited the lowest SIF emission in April (Figure 3a,b).

237 The mean SIF emission over evergreen broadleaf forests was approximately 0.9-1.1 W $m^{-2}$ $\mu m^{-1}$ $sr^{-1}$, whereas those over

238 savannas and grasslands were 0.5-0.7 W $m^{-2}$ $\mu m^{-1}$ $sr^{-1}$ and less than 0.1 W $m^{-2}$ $\mu m^{-1}$ $sr^{-1}$, respectively (Figure 3c,d).

239 Furthermore, we also found a significant difference in the SIF emission intensity over tropical savannas, which was observed

240 by both satellites (Figure 3c,d).

241

242
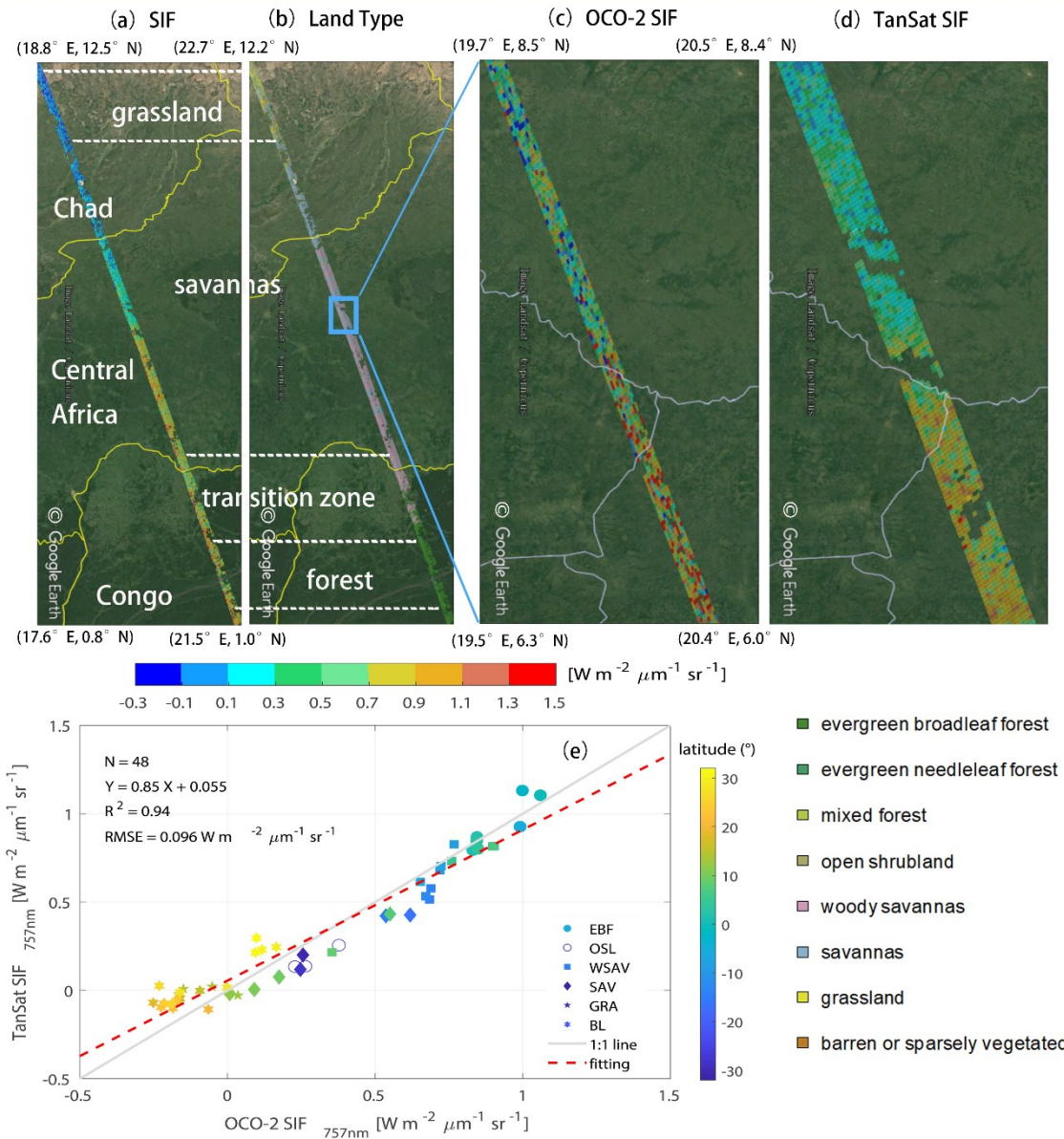
Figure 3: Overlapping orbits of TanSat and OCO-2 on April 19, 2017 over Africa displayed in Google Earth, (a) the SIF measurements from both ~~the two~~ satellites and (b) the footprint land cover type were compared. Compared to OCO-2, TanSat has a wider swath width. A zoom-in view over savannas shows variations in the SIF signal measured by (c) OCO-2 and (d) TanSat. The land surface image shown in Google earth is provided by Landsat/Copernicus team. Following the International Geosphere-Biosphere Programme classification scheme, the vertical legend on the bottom right corner depicts the land cover type that occurs in the study area. The middle horizontal color bar represents the intensity of the SIF radiance. (e) Small-area SIF comparison between OCO-2 and TanSat; each data point represents the mean SIF of a degree in latitude (colors) along the track. The marker legend that is shown on the bottom right of the plot indicates the dominant land cover (defined as the majority land cover type of each sounding) in each small area. There are six land cover types including evergreen broadleaf forest (EBF), open shrubland (OSL), woody savanna (WSAV), savanna (SAV), grassland (GRA), and barren land (BL). The red dashed line represents the linear fit between the two SIF products with statistics shown in the upper left of the plot. The gray line indicates a 1:1 relationship for reference.

256

257 Because the footprint sizes of the two satellites are different, it is difficult to make a direct footprint-to-footprint comparison.

258 Therefore, we made the comparison between the two satellite measurements based on a small area average. Each small area

259 spans a degree in latitude and continues along the track. The small area-averaged SIF comparison is shown in Figure 3e. The

260 results indicate good agreement, with an $R^2$ of 0.94 and an RMSE of 0.096 W m$^{-2}$ μm$^{-1}$ sr$^{-1}$. Additional ground-based SIF

261 measurement setups (Guanter et al., 2007; Liu et al., 2019; van der Tol et al., 2016; Yang et al., 2015a; Yu et al., 2019)

262 should allow for direct evaluation of satellite retrieval accuracy in the future.

263
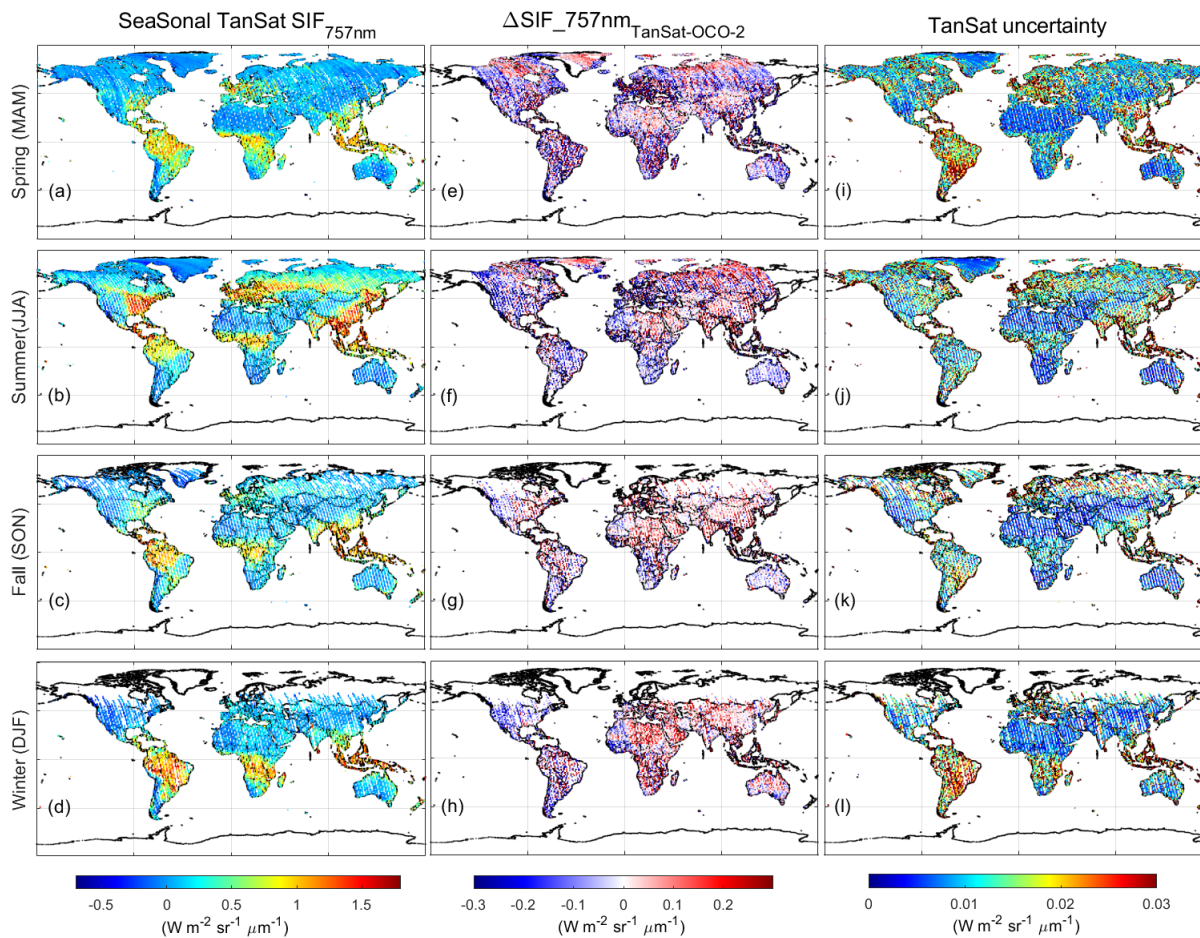


264

265 **Figure 4: Global TanSat SIF (left, a-d), differences between TanSat and IAPCAS OCO-2 SIF values (middle, e-h), and the grid-**
266 **cell retrieval uncertainty estimated from TanSat (right, i-l) at 1° × 1° spatial resolution. The maps in each row represent a**
267 **Northern Hemisphere season, i.e., spring (MAM), summer (JJA), fall (SON), and winter (DJF).**

268

269  Figure 4 shows the global SIF comparison between IAPCAS/SIF retrieved OCO-2 and TanSat; this comparison is only

270  performed at $1° \times 1°$ spatial resolution. In general, the difference in SIF globally is mostly less than 0.3 W m$^{-2}$ μm$^{-1}$ sr$^{-1}$ for

271  all seasons, and on average, the smallest difference appears in fall. There are regional biases observed in North Africa, South

272  Africa, South America, and Europe in all seasons except fall. This is mainly caused by the differences in instrument

273  performance between TanSat and OCO-2, such as the Instrument Respond Function and the Signal-to-Noise. The instrument

274  performance difference is represented by the different structural characteristics of the bias curves. The bias correction

275  compensates for most of the bias caused by instrument performance; however, small biases could remain. Furthermore, the

276  hundreds of kilometers of distance between the OCO-2 and TanSat footprints, for example, over different vegetation regions,

277  will also cause some measurement discrepancies. The global distribution of the two satellites was also compared with the

278  official OCO-2 SIF data on the global scale, the results show that the difference between the retrieved SIF maps and the

279  official map is less than 0.2 W m$^{-2}$ μm$^{-1}$ sr$^{-1}$, indicating that the retrieved SIF data from OCO-2 and TanSat both have good

280  SIF characterization capabilities on a global scale. The uncertainty σ of each sounding was estimated to validate SIF

281  reliability and is provided in the product. σ is derived from the retrieval error covariance matrix, $S_e = (K^T S_0^{-1} K)^{-1}$, where $K$

282  is the Jacobian matrix from the forward model fitting and $S_0$ is the measurement error covariance matrix that is calculated

283  from the instrument spectrum noise. In general, σ ranges from 0.1 to 0.6 W m$^{-2}$ μm$^{-1}$ sr$^{-1}$ for both TanSat and OCO-2

284  measurements in the 757 nm fitting window, which is of a similar magnitude and data range as those of previous studies (Du

285  et al., 2018; Frankenberg et al., 2014a). Meanwhile, the standard error of the mean SIF in each grid $\sigma_{meas}$ was estimated to

286  represent the gridded retrieval error and natural variability, which is calculated from TanSat SIF values with $\sigma_{meas} = \frac{\sigma_{std}}{\sqrt{n}}$

287  and $\sigma_{std} = \sqrt{\frac{\sum_{i=1}^{n}(SIF_i - \overline{SIF})^2}{n}}$, where $\sigma_{std}$ represents the standard deviation of the grid cell with $n$ soundings, $SIF_i$ is the

288  retrieved SIF values of each sounding, and $\overline{SIF}$ is the mean SIF value for all measurements in the grid. As depicted in the

289  right column of Figure 4, the $\sigma_{meas}$ of each grid cell is much lower than the precision of a single sounding. The $\sigma_{meas}$ for

290  South America is larger than that for any other region on the globe (Figure 4i-l). This is similar to that of OCO-2 SIF

291  retrieval and caused by fewer effective measurements due to the South Atlantic Anomaly (Sun et al., 2018). The difference

292  in SIF emission values between the two satellites indicates that the collaborative usage of two satellite SIF products still

293  requires analysis of the impact of instrument differences, although the two satellite SIF products share the same

294  spatiotemporal pattern on a global scale.

## 3.2 SIF Global Distribution and Temporal Variation

296  The SIF emission intensity reflects the growth status of vegetation ~~due to its correlation with photosynthetic efficiency~~;

297  hence, the overall global vegetation status can be represented by global SIF maps for each season. TanSat SIF over a whole

298  year's cycle, from March 2017 to February 2018, is represented seasonally as a $1° \times 1°$ grid spatially. The seasonal variation

299  in SIF emission is clear in the Northern Hemisphere, i.e., it is enhanced from spring to summer and then decreases (Sun et al.,

300  2018).

301  In general, the SIF emission varied with latitude and the vegetation-covered areas near the equator maintained a continuous

302  SIF emission throughout the year. Large SIF emissions in the Northern Hemisphere, above 1.5 W m$^{-2}$ μm$^{-1}$ sr$^{-1}$, mostly from

303  the eastern U.S., southeast of China, and southern Asia in summer, were due to the large areas of cropland. There was also

304  an obvious SIF emission of 1-1.2 W m$^{-2}$ μm$^{-1}$ sr$^{-1}$ observed over Central Europe and northeastern China during the summer.

305  In these regions, croplands and deciduous forests contribute to SIF emissions. In the Southern Hemisphere, the strongest SIF

306  emission occurred in the Amazon, with a level of approximately 1-2 W m$^{-2}$ μm$^{-1}$ sr$^{-1}$ in DJF (Northern Hemisphere winter),

307  where there is an evergreen broadleaf rainforest. Africa, which is covered by evergreen broadleaf rainforests and woody

308  savannas, had an average SIF value of 0.7-1.5 W m$^{-2}$ μm$^{-1}$ sr$^{-1}$ during the year.

309  The SIF-GPP relationship over different vegetation types was also investigated by comparing the annual mean satellite SIF

310  measurements with the FLUXCOM GPP (Jung et al., 2020; Tramontana et al., 2016) dataset in a 1° × 1° grid over the globe.

311  The FLUXCOM GPP dataset used in the study comprises monthly global gridded flux products with remote sensing and

312  meteorological/climate forcing (RS+METEO) setups, which are derived from mean seasonal cycles according to MODIS

313  data and daily meteorological information (Jung et al., 2020; Tramontana et al., 2016). In the correlation analysis, the high

314  spatial resolution (0.5°× 0.5°) of the FLUXCOM GPP was first resampled to 1°× 1° to keep the same temporal-spatial scale

315  of SIF and GPP data. The satellite-measured SIF is an instantaneous emission signal that varies with incident solar radiance

316  within the day. To reduce the differences caused by the observation time and SZA at different latitudes, we applied a daily

317  adjustment factor to convert the instantaneous SIF emission into a daily mean SIF (Du et al., 2018; Frankenberg et al., 2011b;

318  Sun et al., 2018). The daily adjustment factor d is calculated as follows:

319  $$d = \frac{\int_{t=t_0-12h}^{t=t_0+12h} \cos(SZA(t)) \cdot dt}{\cos(SZA(t_0))} \tag{5}$$

320  where $t_0$ is the observation time in fractional days and $SZA(t)$ is a function of latitude, longitude, and time for calculating

321  the SZA of the measurements. The annual averaged SIF is calculated from the daily mean SIF. To evaluate the relationship

322  between SIF and GPP on the periodic scale of vegetation growth status, annually-averaged data were used in the regression

323  fitting analysis.
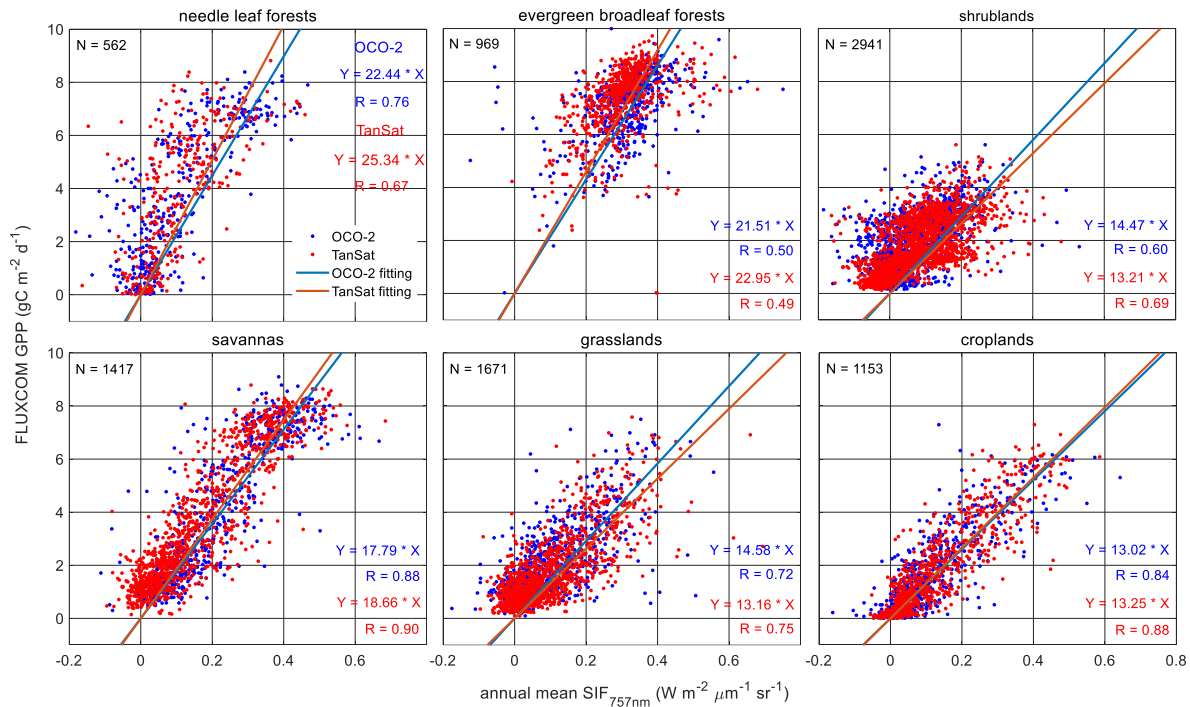
**Figure 5: Relationship between annual mean SIF and FLUXCOM gross primary production (GPP) from March 2017 to February 2018. Blue and red dots represent OCO-2 and TanSat SIF grids, respectively. Fitted lines and statistics for OCO-2 and TanSat are shown in each plot.**

Figure 5 shows the linear fits for six vegetation types, including needle leaf forest, evergreen broadleaf forest, shrubland, savanna, grassland, and cropland. Recent studies have shown a strong linear correlation between SIF and GPP. The TanSat SIF and the OCO-2 official SIF data were used to estimate the SIF-GPP correlation. To make a direct comparison of the relationship between SIF and GPP among various vegetation types, we used non-offset linear fitting to indicate the correlation between satellite SIF and FLUXCOM GPP. For savanna and cropland, there were strong relationships between the mean SIF and GPP with an R-value above 0.84. The fitting results show that the SIF products of the two satellites have similar capabilities in characterizing GPP, especially for the evergreen broadleaf forest, savanna, and cropland, with slopes of approximately 21, 18, and 13, respectively. For shrubland and grassland, the slope of OCO-2 SIF with GPP is higher than that of TanSat and has a worse correlation. For forests, OCO-2 SIF presents a better correlation with GPP, especially in the needle leaf forest. As a whole, for the same vegetation type, the SIF-GPP correlations for the two satellites are rather similar, indicating that the two satellite SIF products have similar capabilities in characterizing GPP. It shows the strong feasibility of the comprehensive application of different satellite SIF products. For different vegetation types, the SIF-GPP correlations were significantly different, indicating the different ability of SIF to characterize GPP of different vegetation. It represents that vegetation type is a key factor in determining the SIF-GPP relationship. The markedly different fitting slopes across various biomes suggest that the application of SIF in GPP estimation needs more detailed analysis although the evidence of the strong linear relationship between them.

14

## 4 Conclusions

In this paper, we introduced the retrieval algorithm IAPCAS/SIF and its application in TanSat and OCO-2 measurements. One-year (March 2017-February 2018) TanSat SIF data was introduced and compared with OCO-2 measurements in this study. The TanSat and OCO-2 SIF products based on the IAPCAS/SIF algorithm are available on the Cooperation on the Analysis of carbon SAtellites data (CASA) website, www.chinageoss.org/tansat. Comparisons between TanSat and OCO-2 measurements directly, using a case study, and indirectly, with global $1°×1°$ grid data, showed consistency between the two satellite missions, indicating that the coordinated usage of the two data products is possible in future studies. The correlation analysis between SIF and GPP further verified the feasibility of the comprehensive application of SIF products from different satellite missions. Meanwhile, it should be noticed that the difference in the ability of satellite SIF products to characterize different vegetation types in data applications. With increasing satellites becoming available for SIF observations, space-based SIF observations have recently expanded in range to provide broad spatiotemporal coverage. The next-generation Chinese carbon monitoring satellite (TanSat-2) is now in the preliminary design phase, which is designed to be a constellation of six satellites to measure different kinds of greenhouse gases and trace gases in a more efficient way, including $CO_2$, $CH_4$, CO, NOx, as well as SIF. SIF measurements from TanSat-2 will provide global data products over broader coverage areas with less noise. The improvement in the spatiotemporal resolution of SIF data will benefit GPP predictions based on the numerous studies of the linear relationship between SIF and GPP. In future work, the measurement accuracy should be validated directly using ground-based measurements to ensure data quality.

## Data availability

The SIF products of TanSat and OCO-2 by IAPCAS/SIF algorithm are available on the Cooperation on the Analysis of carbon SAtellites data (CASA) website (www.chinageoss.org/tansat).


## Author contributions

L.Y. and D.Y. developed the retrieval algorithm, designed the study, and wrote the paper. Y.L. led the SIF data process and analysis. Y.L., D.Y., Z.C., and J.W. contributed to manuscript organization and revision. C.L. and Y.Z. provided information on the TanSat instrument performance. L.T. provided TanSat in-flight information. M.W. and S.W. provided information on the scientific requirement for data further application. N.L. and D.L. led the TanSat data application. Z.Y. led the TanSat in-flight operation.

## References

Boesche, E., Stammes, P., and Bennartz, R.: Aerosol influence on polarization and intensity in near-infrared $O_2$ and $CO_2$ absorption bands observed from space, J. Quant. Spectrosc. Radiat. Transf., 110, 223–239, https://doi.org/10.1016/j.jqsrt.2008.09.019, 2009.

Butz, A., Guerlet, S., Hasekamp, O., Schepers, D., Galli, A., Aben, I., Frankenberg, C., Hartmann, J. M., Tran, H., Kuze, A., Keppel-Aleks, G., Toon, G., Wunch, D., Wennberg, P., Deutscher, N., Griffith, D., MacAtangay, R., Messerschmidt, J., Notholt, J., and Warneke, T.: Toward accurate $CO_2$ and $CH_4$ observations from GOSAT, Geophys. Res. Lett., 38, 2–7, https://doi.org/10.1029/2011GL047888, 2011.

Butz, A., Hasekamp, O. P., Frankenberg, C., and Aben, U.: Retrievals of atmospheric $CO_2$ from simulated space-borne measurements of backscattered near-infrared sunlight: Accounting for aerosol effects, Appl. Opt., 48, 3322–3336, https://doi.org/10.1364/AO.48.003322, 2009.

Butz, A., Hasekamp, O. P., Frankenberg, C., Vidot, J., and Aben, I.: $CH_4$ retrievals from space-based solar backscatter measurements: Performance evaluation against simulated aerosol and cirrus loaded scenes, J. Geophys. Res. Atmos., 115, 1–15, https://doi.org/10.1029/2010JD014514, 2010.

Cai, Z. N., Liu, Y., and Yang, D. X.: Analysis of XCO2 retrieval sensitivity using simulated Chinese Carbon Satellite (TanSat) measurements, Sci. China Earth Sci., 57, 1919–1928, https://doi.org/10.1007/s11430-013-4707-1, 2014.

398  Chen, A., Mao, J., Ricciuto, D., Xiao, J., Frankenberg, C., Li, X., Thornton, P. E., Gu, L., and Knapp, A. K.: Moisture
399  availability mediates the relationship between terrestrial gross primary production and solar-induced chlorophyll
400  fluorescence: Insights from global-scale variations, Glob. Chang. Biol., 1–13, https://doi.org/10.1111/gcb.15373, 2020.

401  Doughty, R., Köhler, P., Frankenberg, C., Magney, T. S., Xiao, X., Qin, Y., Wu, X., and Moore, B.: TROPOMI reveals dry-
402  season increase of solar-induced chlorophyll fluorescence in the Amazon forest, Proc. Natl. Acad. Sci. U. S. A., 116, 22393–
403  22398, https://doi.org/10.1073/pnas.1908157116, 2019.

404  Drusch, M., Moreno, J., del Bello, U., Franco, R., Goulas, Y., Huth, A., Kraft, S., Middleton, E. M., Miglietta, F.,
405  Mohammed, G.: The FLuorescence EXplorer Mission Concept—ESA's Earth Explorer 8, ITGRS, 55, 1273–1284,
406  http://doi.org./10.1109/TGRS.2016.2621820, 2017.

407  Du, S., Liu, L., Liu, X., Zhang, X., Zhang, X., Bi, Y., and Zhang, L.: Retrieval of global terrestrial solar-induced chlorophyll
408  fluorescence from TanSat satellite, Sci. Bull., 63, 1502–1512, https://doi.org/10.1016/j.scib.2018.10.003, 2018.

409  Frankenberg, C., Butz, A., and Toon, G. C.: Disentangling chlorophyll fluorescence from atmospheric scattering effects in
410  $O_2$ A-band spectra of reflected sunlight, Geophys. Res. Lett., 38, 1–5, https://doi.org/10.1029/2010GL045896, 2011a.

411  Frankenberg, C., Fisher, J. B., Worden, J., Badgley, G., Saatchi, S. S., Lee, J. E., Toon, G. C., Butz, A., Jung, M., Kuze, A.,
412  and Yokota, T.: New global observations of the terrestrial carbon cycle from GOSAT: Patterns of plant fluorescence with
413  gross primary productivity, Geophys. Res. Lett., 38, 1–6, https://doi.org/10.1029/2011GL048738, 2011b.

414  Frankenberg, C., O'Dell, C., Berry, J., Guanter, L., Joiner, J., Köhler, P., Pollock, R., and Taylor, T. E.: Prospects for
415  chlorophyll fluorescence remote sensing from the Orbiting Carbon Observatory-2, Remote Sens. Environ., 147, 1–12,
416  https://doi.org/10.1016/j.rse.2014.02.007, 2014a.

417  Frankenberg, C., O'Dell, C., Guanter, L., and McDuffie, J.: Remote sensing of near-infrared chlorophyll fluorescence from
418  space in scattering atmospheres: Implications for its retrieval and interferences with atmospheric CO 2 retrievals, Atmos.
419  Meas. Tech., 5, 2081–2094, https://doi.org/10.5194/amt-5-2081-2012, 2012.

420  Frankenberg, C.: OCO-2 Algorithm Theoretical Basis Document: IMAP-DOAS pre-processor, 2014b.

421  Guanter, L., Aben, I., Tol, P., Krijger, J. M., Hollstein, A., Köhler, P., Damm, A., Joiner, J., Frankenberg, C., and Landgraf,
422  J.: Potential of the TROPOspheric Monitoring Instrument (TROPOMI) onboard the Sentinel-5 Precursor for the monitoring
423  of terrestrial chlorophyll fluorescence, https://doi.org/10.5194/amt-8-1337-2015, 2015.

424  Guanter, L., Alonso, L., Gómez-Chova, L., Amorós-López, J., Vila, J., and Moreno, J.: Estimation of solar-induced
425  vegetation fluorescence from space measurements, Geophys. Res. Lett., 34, 1–5, https://doi.org/10.1029/2007GL029289,
426  2007.

427  Guanter, L., Frankenberg, C., Dudhia, A., Lewis, P. E., Gómez-Dans, J., Kuze, A., Suto, H., and Grainger, R. G.: Retrieval
428  and global assessment of terrestrial chlorophyll fluorescence from GOSAT space measurements, Remote Sens. Environ., 121,
429  236–251, https://doi.org/10.1016/j.rse.2012.02.006, 2012.

430  Guanter, L., Zhang, Y., Jung, M., Joiner, J., Voigt, M., Berry, J. A., Frankenberg, C., Huete, A. R., Zarco-Tejada, P., Lee, J.
431  E., Moran, M. S., Ponce-Campos, G., Beer, C., Camps-Valls, G., Buchmann, N., Gianelle, D., Klumpp, K., Cescatti, A.,

432  Baker, J. M., and Griffis, T. J.: Global and time-resolved monitoring of crop photosynthesis with chlorophyll fluorescence,

433  Proc. Natl. Acad. Sci. U. S. A., 111, https://doi.org/10.1073/pnas.1320008111, 2014.

434  Joiner, J., Guanter, L., Lindstrot, R., Voigt, M., Vasilkov, A. P., Middleton, E. M., Huemmrich, K. F., Yoshida, Y., and

435  Frankenberg, C.: Global monitoring of terrestrial chlorophyll fluorescence from moderate-spectral-resolution near-infrared

436  satellite measurements: methodology, simulations, and application to GOME-2, Atmos. Meas. Tech., 6, 2803–2823,

437  https://doi.org/10.5194/amt-6-2803-2013, 2013.

438  Joiner, J., Yoshida, Y., Guanter, L., and Middleton, E. M.: New methods for the retrieval of chlorophyll red fluorescence

439  from hyperspectral satellite instruments: simulations and application to GOME-2 and SCIAMACHY, Atmos. Meas. Tech., 9,

440  3939–3967, https://doi.org/10.5194/amt-9-3939-2016, 2016.

441  Joiner, J., Yoshida, Y., Vasilkov, A. P., Middleton, E. M., Campbell, P. K. E., Yoshida, Y., Kuze, A., and Corp, L. A.:

442  Filling-in of near-infrared solar lines by terrestrial fluorescence and other geophysical effects: simulations and space-based

443  observations from SCIAMACHY and GOSAT, Atmos. Meas. Tech., 5, 809–829, https://doi.org/10.5194/amt-5-809-2012,

444  2012.

445  Joiner, J., Yoshida, Y., Vasilkov, A. P., Yoshida, Y., Corp, L. A., and Middleton, E. M.: First observations of global and

446  seasonal terrestrial chlorophyll fluorescence from space, 8, 637–651, https://doi.org/10.5194/bg-8-637-2011, 2011.

447  Joiner, J., Yoshida, Y., Zhang, Y., Duveiller, G., Jung, M., Lyapustin, A., Wang, Y., and Tucker, C. J.: Estimation of

448  terrestrial global gross primary production (GPP) with satellite data-driven models and eddy covariance flux data, Remote

449  Sens., 10, 1–38, https://doi.org/10.3390/rs10091346, 2018.

450  Jung, M., Schwalm, C., Migliavacca, M., Walther, S., Camps-Valls, G., Koirala, S., Anthoni, P., Besnard, S., Bodesheim, P.,

451  Carvalhais, N., Chevallier, F., Gans, F., S Goll, D., Haverd, V., Köhler, P., Ichii, K., K Jain, A., Liu, J., Lombardozzi, D., E

452  M S Nabel, J., A Nelson, J., O'Sullivan, M., Pallandt, M., Papale, D., Peters, W., Pongratz, J., Rödenbeck, C., Sitch, S.,

453  Tramontana, G., Walker, A., Weber, U., and Reichstein, M.: Scaling carbon fluxes from eddy covariance sites to globe:

454  Synthesis and evaluation of the FLUXCOM approach, 17, 1343–1365, https://doi.org/10.5194/bg-17-1343-2020, 2020.

455  Köhler, P., Frankenberg, C., Magney, T. S., Guanter, L., Joiner, J., and Landgraf, J.: Global Retrievals of Solar-Induced

456  Chlorophyll Fluorescence With TROPOMI: First Results and Intersensor Comparison to OCO-2, Geophys. Res. Lett., 45,

457  10,456-10,463, https://doi.org/10.1029/2018GL079031, 2018b.

458  Köhler, P., Guanter, L., and Joiner, J.: A linear method for the retrieval of sun-induced chlorophyll fluorescence from

459  GOME-2 and SCIAMACHY data, Atmos. Meas. Tech., 8, 2589–2608, https://doi.org/10.5194/amt-8-2589-2015, 2015.

460  Köhler, P., Guanter, L., Kobayashi, H., Walther, S., and Yang, W.: Assessing the potential of sun-induced fluorescence and

461  the canopy scattering coefficient to track large-scale vegetation dynamics in Amazon forests, Remote Sens. Environ., 204,

462  769–785, https://doi.org/10.1016/j.rse.2017.09.025, 2018a.

463  Lee, J. E., Frankenberg, C., Van Der Tol, C., Berry, J. A., Guanter, L., Boyce, C. K., Fisher, J. B., Morrow, E., Worden, J. R.,

464  Asefi, S., Badgley, G., and Saatchi, S.: Forest productivity and water stress in Amazonia: Observations from GOSAT

465  chlorophyll fluorescence, Tohoku J. Exp. Med., 230, https://doi.org/10.1098/rspb.2013.0171, 2013.

Li, X., Xiao, J., and He, B.: Chlorophyll fluorescence observed by OCO-2 is strongly related to gross primary productivity estimated from flux towers in temperate forests, Remote Sens. Environ., 204, 659–671, https://doi.org/10.1016/j.rse.2017.09.034, 2018.

Li, X., Xiao, J., Kimball, J. S., Reichle, R. H., Scott, R. L., Litvak, M. E., Bohrer, G., and Frankenberg, C.: Synergistic use of SMAP and OCO-2 data in assessing the responses of ecosystem productivity to the 2018 U.S. drought, Remote Sens. Environ., 251, 112062, https://doi.org/10.1016/j.rse.2020.112062, 2020.

Liu, X., Guanter, L., Liu, L., Damm, A., Malenovský, Z., Rascher, U., Peng, D., Du, S., and Gastellu-Etchegorry, J. P.: Downscaling of solar-induced chlorophyll fluorescence from canopy level to photosystem level using a random forest model, Remote Sens. Environ., 231, 110772, https://doi.org/10.1016/j.rse.2018.05.035, 2019.

Liu, Y., Wang, J., Yao, L., Chen, X., Cai, Z., Yang, D., Yin, Z., Gu, S., Tian, L., Lu, N., and Lyu, D.: The TanSat mission: preliminary global observations, Sci. Bull., 63, 1200–1207, https://doi.org/10.1016/j.scib.2018.08.004, 2018.

MacBean, N., Maignan, F., Bacour, C., Lewis, P., Peylin, P., Guanter, L., Köhler, P., Gómez-Dans, J., and Disney, M.: Strong constraint on modelled global carbon uptake using solar-induced chlorophyll fluorescence data, Sci. Rep., 8, 1–12, https://doi.org/10.1038/s41598-018-20024-w, 2018.

O'Dell, C. W., Connor, B., Bösch, H., O'Brien, D., Frankenberg, C., Castano, R., Christi, M., Eldering, D., Fisher, B., Gunson, M., McDuffie, J., Miller, C. E., Natraj, V., Oyafuso, F., Polonsky, I., Smyth, M., Taylor, T., Toon, G. C., Wennberg, P. O., and Wunch, D.: The ACOS $CO_2$ retrieval algorithm-Part 1: Description and validation against synthetic observations, Atmos. Meas. Tech., 5, 99–121, https://doi.org/10.5194/amt-5-99-2012, 2012.

Qiu, R., Han, G., Ma, X., Xu, H., Shi, T., and Zhang, M.: A comparison of OCO-2 SIF, MODIS GPP, and GOSIF data from gross primary production (GPP) estimation and seasonal cycles in North America, Remote Sens., 12, https://doi.org/10.3390/rs12020258, 2020.

Reuter, M., Buchwitz, M., Schneising, O., Heymann, J., Bovensmann, H., and Burrows, J. P.: A method for improved SCIAMACHY $CO_2$ retrieval in the presence of optically thin clouds, Atmos. Meas. Tech., 3, 209–232, https://doi.org/10.5194/amt-3-209-2010, 2010.

Sun, K., Liu, X., Nowlan, C. R., Cai, Z., Chance, K., Frankenberg, C., Lee, R. A. M., Pollock, R., Rosenberg, R., and Crisp, D.: Characterization of the OCO-2 instrument line shape functions using on-orbit solar measurements, Atmos. Meas. Tech., 10, 939–953, https://doi.org/10.5194/amt-10-939-2017, 2017b.

Sun, Y., Frankenberg, C., Jung, M., Joiner, J., Guanter, L., Köhler, P., and Magney, T.: Overview of Solar-Induced chlorophyll Fluorescence (SIF) from the Orbiting Carbon Observatory-2: Retrieval, cross-mission comparison, and global monitoring for GPP, Remote Sens. Environ., 209, 808–823, https://doi.org/10.1016/j.rse.2018.02.016, 2018.

Sun, Y., Frankenberg, C., Wood, J. D., Schimel, D. S., Jung, M., Guanter, L., Drewry, D. T., Verma, M., Porcar-Castell, A., Griffis, T. J., Gu, L., Magney, T. S., Köhler, P., Evans, B., and Yuen, K.: OCO-2 advances photosynthesis observation from space via solar-induced chlorophyll fluorescence, Science (80-. )., 358, https://doi.org/10.1126/science.aam5747, 2017a.

Sun, Y., Fu, R., Dickinson, R., Joiner, J., Frankenberg, C., Gu, L., Xia, Y., and Fernando, N.: Drought onset mechanisms revealed by satellite solar-induced chlorophyll fluorescence: Insights from two contrasting extreme events, J. Geophys. Res. G Biogeosciences, 120, 2427–2440, https://doi.org/10.1002/2015JG003150, 2015.

Tramontana, G., Jung, M., Schwalm, C. R., Ichii, K., Camps-Valls, G., Ráduly, B., Reichstein, M., Arain, M. A., Cescatti, A., Kiely, G., Merbold, L., Serrano-Ortiz, P., Sickert, S., Wolf, S., and Papale, D.: Predicting carbon dioxide and energy fluxes across global FLUXNET sites with regression algorithms, 13, 4291–4313, https://doi.org/10.5194/bg-13-4291-2016, 2016.

van der Tol, C., Rossini, M., Cogliati, S., Verhoef, W., Colombo, R., Rascher, U., and Mohammed, G.: A model and measurement comparison of diurnal cycles of sun-induced chlorophyll fluorescence of crops, Remote Sens. Environ., 186, 663–677, https://doi.org/10.1016/j.rse.2016.09.021, 2016.

Yang, D., Boesch, H., Liu, Y., Somkuti, P., Cai, Z., Chen, X., Di Noia, A., Lin, C., Lu, N., Lyu, D., Parker, R. J., Tian, L., Wang, M., Webb, A., Yao, L., Yin, Z., Zheng, Y., Deutscher, N. M., Griffith, D. W. T., Hase, F., Kivi, R., Morino, I., Notholt, J., Ohyama, H., Pollard, D. F., Shiomi, K., Sussmann, R., Té, Y., Velazco, V. A., Warneke, T., and Wunch, D.: Toward High Precision XCO2 Retrievals From TanSat Observations: Retrieval Improvement and Validation Against TCCON Measurements, J. Geophys. Res. Atmos., 125, 1–26, https://doi.org/10.1029/2020JD032794, 2020.

Yang, D., Liu, Y., Boesch, H., Yao, L., Di Noia, A., Cai, Z., Lu, N., Lyu, D., Wang, M., Wang, J., Yin, Z., and Zheng, Y.: A New TanSat XCO2 Global Product towards Climate Studies, Adv. Atmos. Sci., 38, 8–11, https://doi.org/10.1007/s00376-020-0297-y, 2021.

Yang, D., Liu, Y., Cai, Z., Chen, X., Yao, L., and Lu, D.: First Global Carbon Dioxide Maps Produced from TanSat Measurements, Adv. Atmos. Sci., 35, 621–623, https://doi.org/10.1007/s00376-018-7312-6, 2018.

Yang, D., Liu, Y., Cai, Z., Deng, J., Wang, J., and Chen, X.: An advanced carbon dioxide retrieval algorithm for satellite measurements and its application to GOSAT observations, Sci. Bull., 60, 2063–2066, https://doi.org/10.1007/s11434-015-0953-2, 2015b.

Yang, X., Tang, J., Mustard, J. F., Lee, J. E., Rossini, M., Joiner, J., Munger, J. W., Kornfeld, A., and Richardson, A. D.: Solar-induced chlorophyll fluorescence that correlates with canopy photosynthesis on diurnal and seasonal scales in a temperate deciduous forest, Geophys. Res. Lett., 42, 2977–2987, https://doi.org/10.1002/2015GL063201, 2015a.

Yao, L., Yang, D., Liu, Y., Wang, J., Liu, L., Du, S., Cai, Z., Lu, N., Lyu, D., Wang, M., Yin, Z., and Zheng, Y.: A New Global Solar-induced Chlorophyll Fluorescence (SIF) Data Product from TanSat Measurements, Adv. Atmos. Sci., 38, 341–345, https://doi.org/10.1007/s00376-020-0204-6, 2021.

Yin, Y., Byrne, B., Liu, J., Wennberg, P. O., Davis, K. J., Magney, T., Köhler, P., He, L., Jeyaram, R., Humphrey, V., Gerken, T., Feng, S., Digangi, J. P., and Frankenberg, C.: Cropland Carbon Uptake Delayed and Reduced by 2019 Midwest Floods, AGU Adv., 1, 1–15, https://doi.org/10.1029/2019av000140, 2020.

Yoshida, Y., Joiner, J., Tucker, C., Berry, J., Lee, J. E., Walker, G., Reichle, R., Koster, R., Lyapustin, A., and Wang, Y.: The 2010 Russian drought impact on satellite measurements of solar-induced chlorophyll fluorescence: Insights from

modeling and comparisons with parameters derived from satellite reflectances, Remote Sens. Environ., 166, 163–177, https://doi.org/10.1016/j.rse.2015.06.008, 2015.

Yoshida, Y., Kikuchi, N., Morino, I., Uchino, O., Oshchepkov, S., Bril, A., Saeki, T., Schutgens, N., Toon, G. C., Wunch, D., Roehl, C. M., Wennberg, P. O., Griffith, D. W. T., Deutscher, N. M., Warneke, T., Notholt, J., Robinson, J., Sherlock, V., Connor, B., Rettinger, M., Sussmann, R., Ahonen, P., Heikkinen, P., Kyrö, E., Mendonca, J., Strong, K., Hase, F., Dohe, S., and Yokota, T.: Improvement of the retrieval algorithm for GOSAT SWIR XCO2and XCH4and their validation using TCCON data, Atmos. Meas. Tech., 6, 1533–1547, https://doi.org/10.5194/amt-6-1533-2013, 2013.

Yoshida, Y., Ota, Y., Eguchi, N., Kikuchi, N., Nobuta, K., Tran, H., Morino, I., and Yokota, T.: Retrieval algorithm for $CO_2$ and $CH_4$ column abundances from short-wavelength infrared spectral observations by the Greenhouse gases observing satellite, Atmos. Meas. Tech., 4, 717–734, https://doi.org/10.5194/amt-4-717-2011, 2011.

Yu, L., Wen, J., Chang, C. Y., Frankenberg, C., and Sun, Y.: High-Resolution Global Contiguous SIF of OCO-2, Geophys. Res. Lett., 46, 1449–1458, https://doi.org/10.1029/2018GL081109, 2019.

Zhang, Y., Guanter, L., Berry, J. A., Joiner, J., van der Tol, C., Huete, A., Gitelson, A., Voigt, M., and Köhler, P.: Estimation of vegetation photosynthetic capacity from space-based measurements of chlorophyll fluorescence for terrestrial biosphere models, Glob. Chang. Biol., 20, 3727–3742, https://doi.org/10.1111/gcb.12664, 2014.

Zhang, Y., Xiao, X., Zhang, Y., Wolf, S., Zhou, S., Joiner, J., Guanter, L., Verma, M., Sun, Y., Yang, X., Paul-Limoges, E., Gough, C. M., Wohlfahrt, G., Gioli, B., van der Tol, C., Yann, N., Lund, M., and de Grandcourt, A.: On the relationship between sub-daily instantaneous and daily total gross primary production: Implications for interpreting satellite-based SIF retrievals, Remote Sens. Environ., 205, 276–289, https://doi.org/10.1016/j.rse.2017.12.009, 2018.